Title

Biological Impacts on Carbon Speciation and Morphology of Sea Spray Aerosol

Journal

ACS Earth and Space Chemistry, 1(9)

ISSN

2472-3452

Authors

Pham, Don Q
O'Brien, Rachel
Fraund, Matthew
et al.

Publication Date

2017-11-16

DOI

10.1021/acsearthspacechem.7b00069

Peer reviewed

ACS EARTH AND SPACE CHEMISTRY

Article

Cite This: ACS Earth Space Chem. 2017, 1, 551-561

http://pubs.acs.org/journal/aesccq

Biological Impacts on Carbon Speciation and Morphology of Sea Spray Aerosol

Don Q. Pham,[†] Rachel O'Brien,[†,§,▽] Matthew Fraund,[†] Daniel Bonanno,[†] Olga Laskina,[∥] Charlotte Beall,[#] Kathryn A. Moore,[‡] Sara Forestieri,[⊥] Xiaofei Wang,[‡] Christopher Lee,[‡] Camille Sultana,[‡] Vicki Grassian,[‡] Christopher D. Cappa,[⊥] Kimberly A. Prather,[‡,#] and Ryan C. Moffet*[,†]

[†]Department of Chemistry, University of the Pacific, Stockton, California 95211, United States

[‡]Department of Chemistry and Biochemistry, University of California San Diego, La Jolla, California 92093, United States

[§]Chemical Sciences Division, Lawrence Berkeley National Laboratory, Berkeley, California 94720, United States

[∥]Department of Chemistry, University of Iowa, Iowa City, Iowa 52242, United States

[⊥]Department of Civil and Environmental Engineering, University of California Davis, Davis, California 95616, United States

[#]Scripps Institution of Oceanography, University of California San Diego, La Jolla, California 92037, United States

Supporting Information

ABSTRACT: Sea spray aerosol (SSA) can have complex carbon speciation that is affected by biological conditions in the seawater from which it originates. Biologically derived molecules can also interact with other longer-lived organic and inorganic carbon species in the sea surface microlayer and in the process of bubble bursting. An isolated wave channel facility was used to generate sea spray aerosol during a 1 month mesocosm study. Two consecutive phytoplankton blooms occurred, and sea spray aerosol was sampled throughout. Scanning transmission X-ray microscopy coupled with near-edge X-ray absorption fine structure spectroscopy (STXM-NEXAFS) was used to determine spatially resolved carbon speciation within individual particles from 0.18 to 3.2 μm. During phytoplankton blooms, coarse-mode particles exhibited an increased abundance of carboxylic acid-rich needlelike structures. The extent of organic enrichment in fine-mode particles correlates with the occurrence of aliphatic-rich organic species, as detected by an intense C 1s → σ(C−H)* excitation. These aliphatic-rich species had a strong association with graphitic carbon, as detected by a C 1s → σ* exciton excitation. This enrichment was unique to particles collected in the aerodynamic size range 0.18−0.32 μm and corresponded with the decrease in hygroscopicity. Aliphatic organics can significantly suppress the particle hygroscopicity when they replace salt, thus influencing the effect of sea spray aerosol on light scattering and cloud formation. These results suggest that graphitic carbon is concentrated in the sea surface microlayer during phytoplankton blooms and released through wave action. These results may have implications for radiative transfer and carbon cycling in the ocean−atmosphere system.

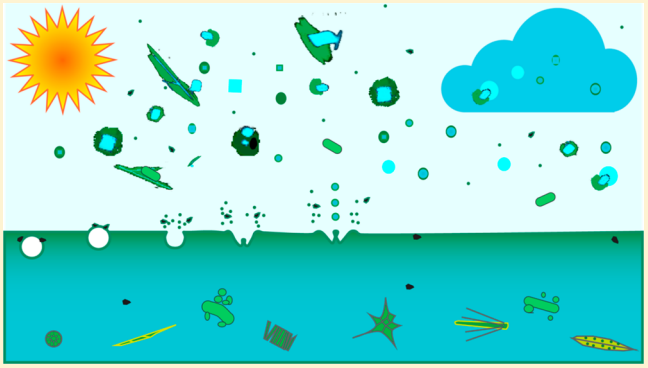

KEYWORDS: *STXM-NEXAFS, sea spray aerosol (SSA), cloud condensation nuclei (CCN), CAICE, IMPACTS*

1. INTRODUCTION

Aerosol particles influence the climate directly by absorbing and scattering light and indirectly by serving as cloud condensation nuclei (CCN).[1,2] Sea spray aerosols (SSAs) contribute roughly to 50% of the global aerosol mass and are expected to make up a significant fraction of CCN.[1] The cloud nucleating activity of atmospheric aerosols is a function of the size and chemical composition of the particles. How the chemical constituents are mixed (termed the "mixing state") plays an important role in both ice nucleation and liquid water uptake.[3,4] Previous studies have shown that SSAs consist of multiple particle types[5,6] and that the degree of mixing between inorganic and organic constituents presented by the different particle types can lead to vastly different hygroscopicities, as characterized by the hygroscopicity parameter κ.[2]

Through the well-known bubble bursting mechanism, organic material is expected to be enriched in smaller-sized SSAs.[7−11] Bubble bursting leads to both film and jet drop formation. Film drops originate from the thin surface film of the bubbles as they burst and are hypothesized to be enriched in surface-active organics through the rising of the bubble.[10]

Received: June 14, 2017
Revised: September 11, 2017
Accepted: September 19, 2017
Published: September 19, 2017

DOI: 10.1021/acsearthspacechem.7b00069
ACS Earth Space Chem. 2017, 1, 551−561

Larger jet drops form from the ejection of water from the resulting cavity and are usually assumed to have a composition more representative of bulk seawater. Film drop formation is widely believed to lead mostly to submicron SSAs, while jet drop formation leads mostly to supermicron SSAs.[10,12] As a result, organic enrichment in SSAs is size-dependent, with the submicron population being enriched in organics. Accurate reproduction of SSA generation in the laboratory requires realistic replication of bubble sizes produced by breaking waves in the ocean.[13,14]

Organic matter in SSAs can be derived from dissolved organic matter (DOM) and particulate organic matter (POM) in seawater. Seawater organic matter consists of labile compounds (i.e., monosaccharaides, proteins, and fatty acids) that are normally at low concentrations in seawater,[15,16] semilabile compounds (i.e., acylated polysaccharides),[15] and refractory compounds expected to be humic substances and carboxylic-rich alicyclic molecules (CRAMs).[17] Of the components that under normal conditions make up DOM, approximately <1% are labile compounds, 10−15% are carbohydrates (as semilabile polysaccharides), 5−25% are refractory humic substances, and 25−40% are high-molecular-weight compounds that include both semilabile and refractory compounds.[12] The semilabile high-molecular-weight compounds are termed hydrolyzable polysaccharides, as the structure is unknown, but the decomposition of such compounds produces individual monosaccharides.[18] The refractory high-molecular-weight compounds include CRAMs, graphitic black carbon from marine sediments,[19] and substances that cannot be hydrolyzed. The concentrations of these compounds in SSAs are regulated through a microbial loop in which microorganisms, including phytoplankton and heterotrophic bacteria, produce and recycle organic matter.[20] It is therefore hypothesized that under differing phytoplankton and heterotrophic bacteria populations, varying concentrations of labile, semilabile, and refractory carbonaceous species are enriched in SSAs through the process of bubble bursting.

During the Investigation into Marine Particle Chemistry and Transfer Science (IMPACTS) campaign, a unique wave chamber facility was employed to study the effects of biological activity on SSA composition. The controlled environment was used to mimic natural aerosol produced during bloom conditions while limiting the effects of confounding variables (e.g., advection of non-SSA particles to the sampling site) present in the ambient marine environment. During the course of this experiment, SSAs were generated via wave breaking while two phytoplankton blooms occurred.[21] In this work, STXM-NEXAFS at the carbon K-edge was used to give morphological and molecular information on SSAs generated during the IMPACTS study. The goal of this study was to relate aerosol chemical composition, morphology, mixing state, and hygroscopicity to seawater composition. This type of information contributes to the improvement of models used to predict the radiative effects of marine aerosols.[9,11,21−23]

2. EXPERIMENTAL SECTION

2.1. Wave Flume. A wave flume (Figure S1) at UC San Diego Scripps Institution of Oceanography was used to simulate breaking oceanic waves and marine aerosol generation. Details of the wave flume and IMPACTS campaign have been published elsewhere,[11,21] and a brief description follows here. Seawater (13 000 L) was taken from the ocean floor at the Scripps Pier in La Jolla, CA, and housed in an isolated wave generating facility. The seawater was filtered through a 50 μm mesh to ensure removal of debris and zooplankton. Guillard's f/2 growth medium (Aquatic Eco-Systems, Apopka, FL) and sodium metasilicate were added to the water to promote phytoplankton growth.[24] The seawater was contained in a 33 m wave channel and illuminated continuously through the glass walls using 5700 K full spectrum fluorescent lights (Full Spectrum Solutions, model 205457). The sealed wave flume was provided with air treated with activated charcoal, potassium permanganate, and HEPA filters. To generate aerosols, a 2 m long metal plate located halfway down the length of the wave flume was angled at 30° starting from the bottom of the channel to simulate the rising of a beach. The wave channel used a hydraulic paddle to generate waves. When the waves approached the simulated rising beach, they broke as a result of the change in the water depth profile. The breaking waves formed bubbles, and then bubble bursting generated aerosols, which were sampled roughly 4 ft from the break through stainless steel tubing (0.5″ o.d.) that connected to the microscopy sampler. Other collocated measurements includes chlorophyll *a* concentration, bacteria and virus counts, level of enzyme activity, ice nucleation counts, and real-time mass spectrometry.

2.2. Sample Collection. Microscopy sampling was routinely carried out each day in 3 h blocks (8:00−11:00, 13:00−16:00, and 18:00−21:00) from July 3 to August 8, 2014. A rotating-stage micro-orifice uniform deposit impactor (MOUDI) (MSP Corp., model 110) was used to collect particles for microscopic analysis. Particles were collected on 1 mm^2 frame size Si_3N_4 windows having a 100 nm film thickness (Silson Ltd., ref no. 11406106) using MOUDI stages 8, 6, and 4, having 50% aerodynamic cut diameters of 0.18, 0.56, and 3.2 μm, respectively. Thus, the collected particles had aerodynamic diameter (D_a) ranges of 0.18−0.32 μm (stage 8), 0.56−1 μm (stage 6), and 1.8−3.2 μm (stage 4). The MOUDI was operated at 72% relative humidity; therefore, the aerosols likely had significant liquid water content upon impaction.

2.3. STXM-NEXAFS. Samples collected with the MOUDI were analyzed using STXM-NEXAFS on beamline 5.3.2.2 at the Advanced Light Source at Lawrence Berkeley National Laboratory. Details of the STXM operation been documented elsewhere[25] and are briefly described here. The STXM chamber was pumped down to 100 mTorr and then backfilled with helium to ∼508 Torr. The sample was raster-scanned at the focal point of the monochromatic X-ray beam, and the transmitted intensity was measured to produce an image. The transmitted X-ray intensity acquired at each energy and position on the sample was converted to optical density (OD) using the Beer−Lambert Law:

$$\mathrm{OD} = \ln(I_0/I) = \mu\rho t \quad (1)$$

where μ is the mass absorption coefficient, ρ is the mass density, and t is the thickness of the sample.[26]

To obtain full spectral stacks at the carbon K-edge, approximately 120 constant-energy images were collected from 278 to 320 eV with a smaller energy step size near the carbon edge (284−290 eV). For maps at the carbon edge, single-energy images at 278 and 320 eV were acquired in order to capture the carbon pre-edge absorption and total carbon, respectively. To map the contribution from atomic oxygen, constant-energy images at 525 and 550 eV were acquired.[27] Single-energy images at 400 and 430 eV were acquired to obtain the contribution from atomic nitrogen.

DOI: 10.1021/acsearthspacechem.7b00069
ACS Earth Space Chem. 2017, 1, 551−561

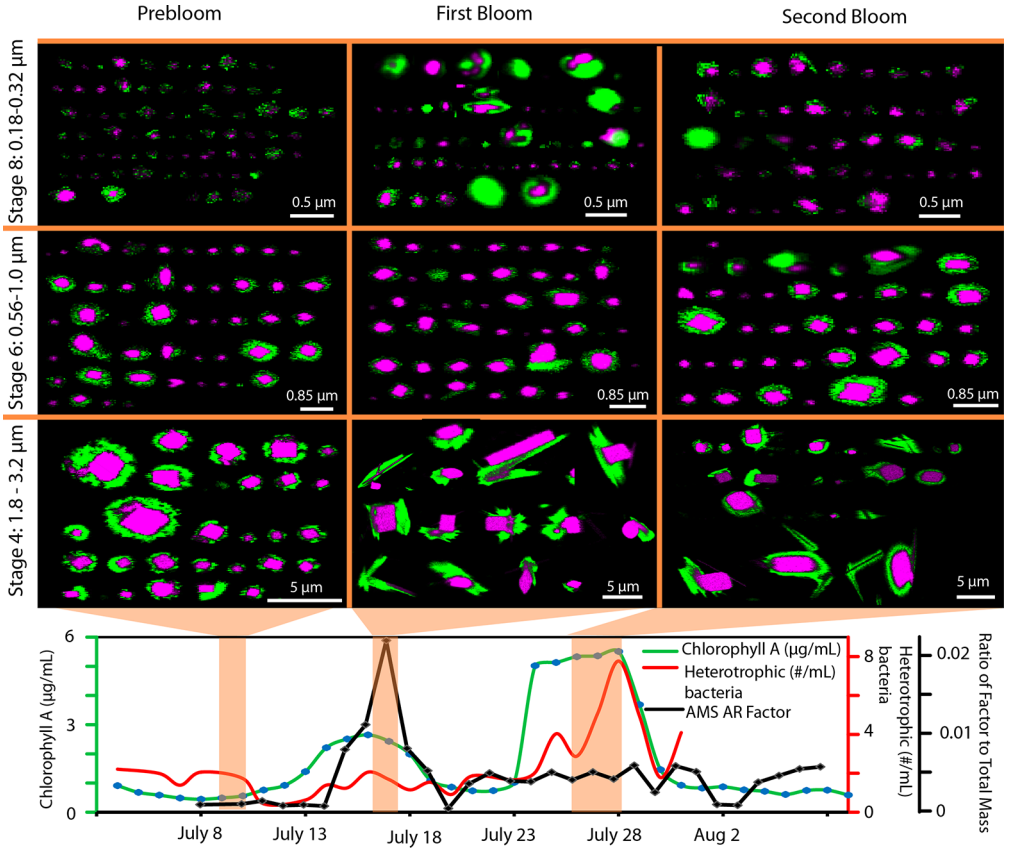

Figure 1. Two-component (green = carbonaceous and purple = noncarbonaceous) singular value decomposition images are shown for all particles analyzed during IMPACTS. Particles are shown as a function of particle size range obtained by the MOUDI aerodynamic diameter cutoffs: 0.18−0.32 μm, 0.56−1 μm, and 1.8−3.2 μm. The orange shading on the time series leading up to the bottom of each image column indicates the time period over which each sample was taken. Particles are also divided by bloom conditions (prebloom, first bloom, and second bloom), which are identified by the chlorophyll *a* time series (bottom). The first bloom shows an overlap with the peak in the relative AR factor mass fraction, while the second bloom shows an overlap with the heterotrophic bacteria concentration.

Particle types were classified through a particle classification decision tree. Organic volume fractions (OVFs) were also determined for individual particles. Details of both methods are discussed in the Supporting Information.

2.4. Peripheral Measurements. Chlorophyll *a* concentrations were measured fluorometrically using a Wetlabs ECO BBFL2 sensor that was calibrated against *Thalassiosira weissflogii* cultures for chlorophyll *a*. Heterotrophic bacteria counts were obtained using epifluorescence microscopy (Keyence model BZ-Z700) after applying SYBR Green I nucleic acid gel stains (Life Technologies, cat. no. S7563).

Bulk dry organic aerosol compositions were measured by high-resolution time-of-flight aerosol mass spectrometry (HR-ToF-AMS); details of these measurements can be found elsewhere.[28] Positive matrix factorization (PMF) was performed on the mass spectrometric data in order to identify two organic component factors: aliphatic-rich (AR) and oxygen-rich (OR).[29]

A cavity ringdown (CRD) spectrometer was used to measure hygroscopic growth factors by measuring extinction at <20% and ~85% relative humidity (RH). Details of the CRD spectrometer can be found elsewhere,[30−32] and its operation is described in the Supporting Information.

3. RESULTS AND DISCUSSION

3.1. Evolution of Particle Morphology. STXM-NEXAFS was used to characterize the particle morphology and chemical composition at the carbon K-edge for three size ranges during three bloom conditions: prebloom, first bloom, and second bloom. Chlorophyll *a* concentrations, heterotrophic bacteria counts, and AMS organic factors were used to characterize the bloom conditions and guide sample selection for microscopy (Figure 1). The prebloom period is representative of seawater conditions in the absence of a phytoplankton bloom, as indicated by the depressed chlorophyll *a* concentrations. The first bloom occurred on July 17 and was characterized by enhanced chlorophyll *a* concentrations, an elevated aliphatic-rich organic component (AR factor, as identified by PMF analysis of AMS data) within the aerosol mass, and relatively low heterotrophic bacteria counts. The second bloom occurred from approximately July 23 to July 28 and was characterized by high chlorophyll *a* concentrations and elevated heterotrophic bacteria counts.[21] For each bloom condition, a two-component singular value decomposition was performed on STXM microscopy particle maps in order to identify phases that could be characterized as predominately carbonaceous or predominately non-carbonaceous (Figure 1).

Care must be taken when interpreting the particle sizes in Figure 1 because they were sampled according to aerodynamic diameter at 72% RH; differences in liquid water content can lead to differences between the aerodynamic diameter at the time of sampling and the geometric diameter under the dry analysis conditions.[33,34] Differences in organic composition and

DOI: 10.1021/acsearthspacechem.7b00069
ACS Earth Space Chem. 2017, 1, 551−561

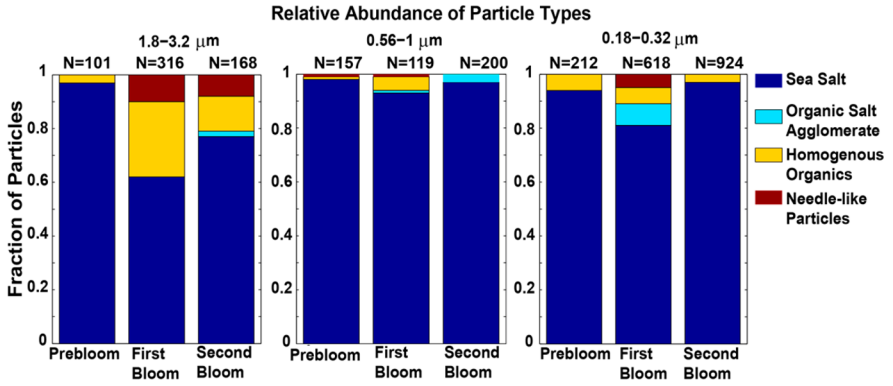

Figure 2. Relative abundances of particle types identified using STXM-NEXAFS: sea salt, homogeneous organics, organic–salt agglomerates, and needlelike particles. For the size range 1.8–3.2 μm, the first and second blooms exhibited fractionary recrystallization and particle shattering, resulting in an increase in particles classified as homogeneous organics and needlelike particles.

morphology can also affect the particle aerodynamic diameter through the following relationship:

$$D_a = D_p\sqrt{\frac{\rho}{\rho_0\chi}} \quad (2)$$

where D_a is the aerodynamic diameter, D_p is the geometric diameter of a spherical particle, ρ is the particle density, ρ_0 is the standard particle density (defined as 1000 kg/m^3), and χ is the dynamic shape factor.[33] From this relationship, a decrease in effective density (ρ/χ) as a result of either an increase in the organic/inorganic ratio or a nonspherical shape leads to an increase in the geometric diameter for the same aerodynamic diameter. Furthermore, because the particles were sampled on flat substrates, further deformation may occur during the impaction process. So-called "particle bounce" may also lead to large particles on the lower stages of the MOUDI.[35]

Although the morphology of these particles resulted from subsequent drying and efflorescence, the observed partitioning of organics and inorganics for individual particles should remain applicable to effloresced aerosols in the environment. For hydrated aerosols, the morphology is expected to be somewhat different because of the increased liquid water content.

For the smallest aerodynamic size range (0.18–0.32 μm), particles during the first bloom were observed to have more carbon-rich phases compared with the second bloom and prebloom periods. The carbon K-edge NEXAFS spectra (section 3.3) indicate that these particles are rich in aliphatic hydrocarbons and graphitic carbon. The increased abundance of AR-carbon-dominant phases during the first bloom is in agreement with the increased relative AR factor mass fraction detected by aerosol mass spectrometry.[21] Possible reasons why the aliphatic-rich particles have larger geometric diameters compared with the hygroscopic inorganic particles are (1) deformation upon impaction, (2) decreased effective density of the aliphatic particles, (3) shrinkage of the hygroscopic inorganic-rich particles, and (4) particle bounce. For intermediate-sized particles (D_a = 0.56–1 μm), there are no major morphological differences between the three bloom conditions. This size range is dominated by particles having salt cores surrounded by an organic coating. The organic phase is slightly thicker for the second bloom, which appears as a slight shift in the OVF distribution, as discussed in section 3.4.

For larger particles in the 1.8–3.2 μm aerodynamic size range, the prebloom period is dominated by sea salt–organic particles having a symmetrical coating of oxidized organics and a clear NaCl core. Organic phases mixed with sea salt are also observed during the first and second bloom periods (Figure 1), but unlike the prebloom period, organics are present in spinelike structures that are identified to contain carboxylic acids, calcium, and potassium (section 3.3). In addition, these particles exhibit a high degree of fractionary recrystallization and particle shattering (section 3.3.2), as indicated by externally mixed organic-rich spines and cubic inorganic salts.[36] Shattering and recrystallization likely occurred during sampling and analysis at low relative humidity. As the blooms progressed, a variety of carboxylic acids with varying carbon chain length and number of carboxylic acid groups were identified, as determined by electrospray ionization high-resolution mass spectrometry (ESI-HR-MS) by Cochran et al.[37] Varying carboxylic acids have different surface activities and affinities for inorganic ions.[38] In this mesocosm experiment, ESI-HR-MS indicated the presence of homologous series of carboxylic acids and dicarboxylic acids with varying degrees of saturation and functional groups (e.g., hydroxyl, oxo), with the average molecular weight distribution of saturated carboxylic acids, for example, decreasing as the mesocosm experiment progressed.[37] Thus, differences in organic composition may explain the changes in particle morphology as the bloom conditions changed for the 1.8–3.2 μm aerodynamic size range.

3.2. Particle Class Abundance. Previous wave flume studies[5,11] showed that there are distinctly different marine aerosol particle types as a function of size, bloom conditions, and available organics. Here it is highlighted that the chemical composition and morphology also change as a function of bloom conditions. To categorize morphologically and chemically distinct particles for statistical analysis, a rule-based algorithm was implemented. These particle classes were optimally separated by using the scheme in Figure S2, and their relative abundances are depicted in Figure 2. Four particle classes were determined through STXM:

1. Sea salt–organic particles with a distinct NaCl core and an organic carbon coating.
2. Homogenous organic particles that contain organic carbon species mixed homogeneously with inorganic species. These particles have an absence of inorganic inclusions and exhibit the spectroscopic and morphological characteristics of marine gels.[5,11,6] For the second bloom, these particles also had a resolved carbonyl peak at 286.6 eV for particles identified as homogeneous organics (Figure S6).

DOI: 10.1021/acsearthspacechem.7b00069
ACS Earth Space Chem. 2017, 1, 551–561

3. Organic salt agglomerates that contain both regions of sea salt and optically thick inclusions of organics resembling bacteria fragments and lipid-rich exudates. The lipid-rich exudates were commonly associated with graphitic black carbon.
4. Needlelike organic-rich particles that contain a calcium-rich spine that can either be calcium sulfate or calcium carbonate. The calcium-rich spine is bordered by carboxylic acid-containing organics as well as potassium.

These particle classes are similar to marine particles observed previously[6,5,39] and have been classified here to enable a quantitative comparison of variations in their relative abundances throughout the duration of IMPACTS. Sea salt−organic was the predominant particle type for all size ranges and bloom conditions, representing 94 ± 6% of particles for prebloom, 83 ± 3% for the first phytoplankton bloom, and roughly 97 ± 3% for the second phytoplankton bloom (Figure 2). The fractional abundance of organic-rich particle types slightly increased during the bloom conditions. It is hypothesized that fractionation and subsequent shattering account for the increase in homogeneous organics and needlelike particles observed for the first and second blooms in the size range 1.8−3.2 μm. Further temporal variations for the different particle types are discussed in detail alongside OVF trends.

3.3. Molecular Characterization of Organic SSA Constituents via NEXAFS Spectroscopy. High-resolution NEXAFS spectra indicated the molecular characteristics of carbon throughout the three bloom conditions. The NEXAFS spectra in Figure 3 represent averages over all carbon-dominant regions and over all particle types for each size range and bloom condition; individual particle spectra for the different particle types are shown in Figure S4. For all of the spectra in Figure 3, contributions from individual transitions were quantified through deconvolution of the carbon K-edge spectrum.[40] Transitions quantified (and indicated in Figure 3) include alkene (C*═C, 285.1 eV), carbonyl (C*═O, 286.7 eV), aliphatic (C*H, 287.7 eV), amide (R−NH(C*═O)R, 288.3 eV), carboxylate (R(C*═O)OH, 288.7 eV), alcohol (C*−OH, 289.5 eV), and carbonate (C^*O_3, 290.4 eV). Figure S5 shows an example of a deconvolution fit to the carbon K-edge. The peak height values for individual transitions shown in the pie graphs in Figure 3 are presented in Table S2. Relative functional group intensities derived from deconvolution are shown as a function of bloom condition and size range to decipher the changes in the organics. Similarly, average spectra and deconvolutions were also obtained for the different particle types (Figures S6 and S7) to demonstrate spectral variation between particle types. As carbonate is the dominant form of carbon in seawater,[15] the C^*O_3 transition at 290.4 eV was observed in most of the spectra. As indicated in Figure 3, the C^*O_3 accounts for 15−22% of the total deconvoluted peak heights. Determining the mass fraction of CO_3^{2-} with respect to total carbon is challenging without the availability of appropriate standards for the organic component. While it is possible for radiation damage to cause the appearance of C^*O_3 in STXM chambers open to the air,[41] this was not observed during the course of these experiments; spectra for standard compounds showed no resolvable contribution from the C^*O_3 transition. Furthermore, the STXM chamber used here was evacuated and backfilled with helium to avoid unwanted reaction of gases with particles in these studies.

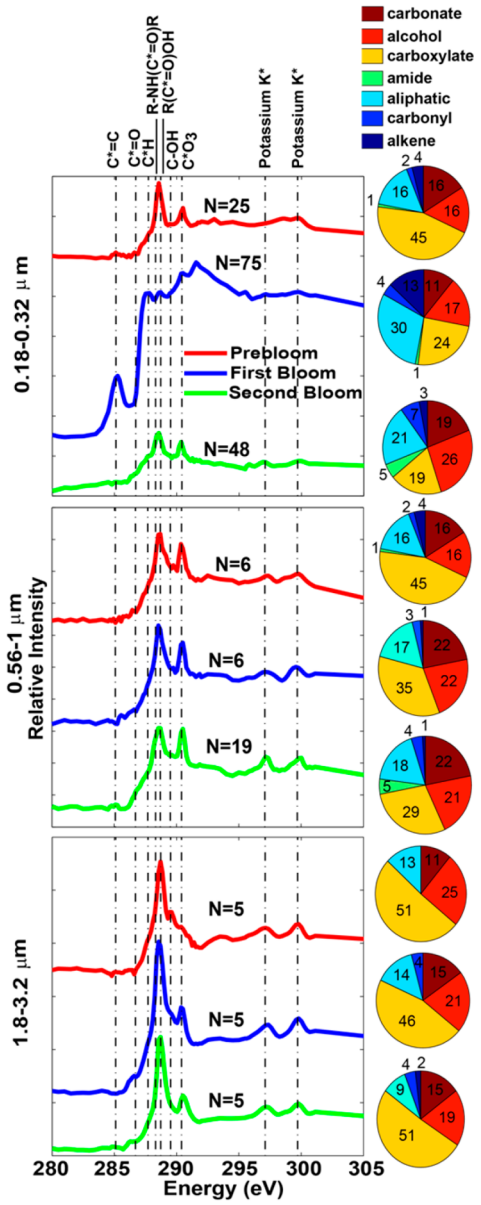

Figure 3. NEXAFS spectra as a function of size range and bloom conditions. The spectra shown result from averaging over all pixels identified as organic-dominant for all particle types for each of the size ranges. Pie charts indicate the results of spectral deconvolution for the functional groups listed. Values are presented as percentages of total peak height of the functional groups listed.

3.3.1. Reduced Aliphatic and Graphitic Carbon. Figure 3 shows that differences in carbon speciation were most noticeable in the 0.18−0.32 μm size range. Aliphatic hydrocarbons were enhanced in the 0.18−0.32 μm size range during first bloom, as indicated by the C*H peak centered around 287.7 eV. These aliphatic hydrocarbons were observed to be internally mixed across multiple particle types (Figure S4). Spectra obtained from these particles resembled previously reported spectra for phospholipids,[42] which are common components of cell walls.[43] The range of the peak absorbance of the carbon C*H from 287.4 to 287.9 eV is indicative of different lengths of hydrocarbons.[44] Identified aliphatics during IMPACTS include fatty acids with carbon chain lengths of C_6−C_{22}.[37] As discussed by Wang et al.,[21] it is hypothesized that aliphatic-rich organic species are transferred into the aerosol

DOI: 10.1021/acsearthspacechem.7b00069
ACS Earth Space Chem. 2017, 1, 551−561

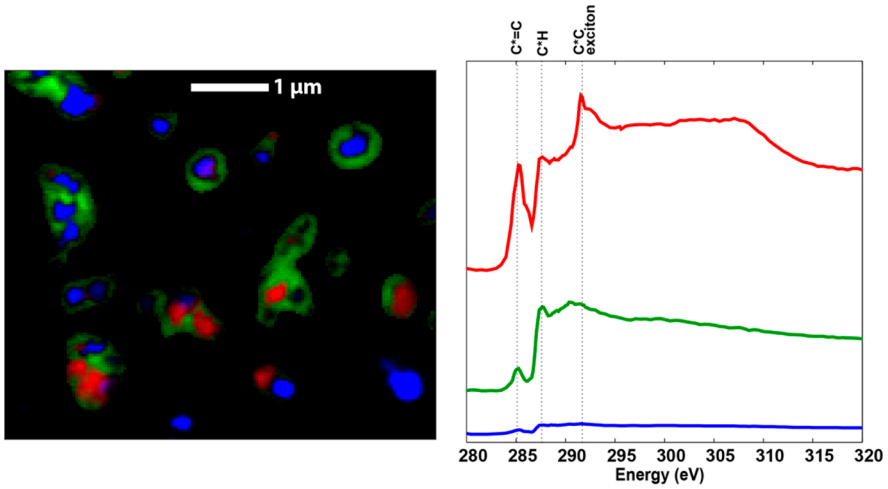

Figure 4. Principal component analysis (PCA) applied to a spectral image acquired at the carbon K-edge for the first bloom for the size range 0.18−0.32 μm. Three unique PCA cluster spectra (right) were used to fit spectral image stack data using singular value decomposition to obtain the image on the left. The red spectrum indicates regions with high contributions from graphitic carbon, while the green spectrum indicates regions rich in aliphatic hydrocarbons. The blue spectrum is indicative of non-carbonaceous inorganic material.

phase via film drops enriched in glyceroglycolipids and phospholipids (structural and functional lipids) and triacylglycerols (energy storage lipids). Other recent Raman spectromicroscopy measurements have confirmed the presence of long-chain fatty acids.[45] These lipids are commonly released into seawater through lysis of phytoplankton cells.[46]

First bloom NEXAFS spectra from the 0.18−0.32 μm size range also indicated a significant increase in the C*═C peak that was spatially correlated with aliphatic hydrocarbons. Principal component analysis revealed a well-defined double resonance near 292 eV indicating inclusions of graphitic carbon (Figure 4, red spectrum). This double resonance is the result of an exciton that yields a sharp peak at 291.5 eV and bandlike contributions leading to the broader peak at 292 eV.[47] Although distinct σ* transitions near these energies have been observed for model phospholipids,[42] the sharp doubly resonant exciton peak is not consistent with assignment to phospholipids. Moreover, the presence of graphitic carbon in these IMPACTS samples was confirmed with Raman spectromicroscopy. Graphitic carbon is a component of marine sediments,[19] and although they are not expected to be abundant in the wave flume, it is possible that fine graphitic carbon particles could have passed through the 50 μm mesh used to filter the seawater. The exclusive enrichment of graphitic carbon to the first bloom, even though the same seawater was used throughout the 31 day experiment, suggests that graphitic carbon has an affinity to aliphatics[19] and appears to be selectively transferred along with aliphatics during the first bloom. These particles, thought to be contamination sources by Prather et al.,[11] may be the result of graphitic carbon being enriched during periods of organic enrichment.

The observation of graphitic carbon internally mixed with aliphatic-rich phases suggests the possibility that graphitic particles may actually be concentrated in the SSML and subsequently emitted from the ocean during particular blooms. Although the transfer of insoluble species has been examined in the past,[48] concentration and emission of graphitic carbon from the SSML is a unique observation with implications for radiative transfer and carbon cycling between the ocean and the atmosphere.

3.3.2. Oxygenated Organic Species. Oxygenated organic species were prevalent throughout the IMPACTS study, in particular for larger size fractions (Figure 3). The main resolved spectral signatures of oxidized carbonaceous particles were those of carboxylic acids and carbonate. The carboxylic acid functionality was prevalent for all spectra and was the dominant feature for prebloom and second bloom particles. The NEXAFS spectral characteristics of highly oxidized organic carbon from these experiments resemble those of carbohydrates and carboxylic acids observed in previous studies of SSA.[6,49]

As the size increases, the contribution from the carboxylic acid peak increases—likely because the oxidized organic material is more soluble and therefore enriched in the larger jet drops. In the smallest size range, the relative contribution from carboxylic acid and carbonate is depressed during the first bloom because of the enhanced contribution from aliphatic organics and graphitic carbon. During the prebloom and second bloom periods, particles in the 0.18−0.32 nm size range had a larger contribution from carboxylic acids but still less than for the larger-sized particles sampled at the same time. The lack of difference in the chemical characteristics in the intermediate 0.56−1.0 μm size range suggests that the organics in these particles are likely a result of water-soluble nonlabile oxidized organics ejected as SSA via the jet drop mechanism. Particles in the largest size range exhibited the largest overall contribution from carboxylic acids compared with smaller sizes. Moreover, as shown in Figure 1, the morphology of these carboxylic acid-rich particles demonstrated a distinct difference under bloom conditions compared with particles sampled during the prebloom period. Strong interactions between carboxylates and calcium can lead to selective enrichment in aerosols.[38,50] Large amounts of carboxylic acid groups were observed coating calcium spines (Figure S3). The inclusions of calcium tend to be rodlike and appear similar in morphology to the calcium sulfate rods identified by Ault et al.[5] Examples of both $CaCO_3$ and $CaSO_4$ spines, confirmed through scanning electron microscopy (SEM) and Raman spectromicroscopy, were identified during IMPACTS. Either composition, however, shows clear structural ordering of carboxylic acid around the calcium spines that are also rich in potassium. The calcium/carboxylic regions do not homogeneously mix with the NaCl/

DOI: 10.1021/acsearthspacechem.7b00069
ACS Earth Space Chem. 2017, 1, 551−561

carboxylic regions in the dry state. The lack of mixing between these phases is characteristic of the high degree of fractionary recrystallization and shattering as well as the increased surfactant behavior of organics under bloom conditions.[36] Fractionary recrystallization was exclusive to only the first bloom and for the size range 1.8−3.2 μm, where an abundance of these calcium/organic spines were observed. Mouri and Okada[36] reported similar calcium sulfate spines resulting from fractionary recrystallization when the Na/Ca or Na/S ratio is high. The resulting spines and shattering occur from separate recrystallization of NaCl and $CaSO_4$ due to solubility differences, which results in loosely attached crystals of NaCl and $CaSO_4$ that readily shatter. Others have implied optical and morphological changes when the carboxylic acid to inorganic ratio increases.[51] These results indicate that biological activity leads to significantly different organic pools that may impact the particle morphology.

3.3.3. Distribution of Amides and Saccharides and Comparison with Model Compounds. The amide group was resolved for prebloom and first bloom particles and was observed exclusively in a few particle inclusions during the second bloom. The source of the amide group is presumably proteinaceous cellular components of bacteria having an *N*-acetyl group. The amide group is associated with organic-rich inclusions observed during the second bloom (Figure S4). The spectrum shown (Figure S4, second bloom, organic salt aggregate) has equal-intensity peaks at 288.3 eV for K 1s → π^* (R−NH(C*═O)R) and 288.7 eV for K 1s → π^* (R(C*═O)OH) consistent with peptidoglycan, a component of bacterial cell membranes.[52]

Other occasionally resolved features of the NEXAFS spectrum are the absorbance at 289.5 eV for K 1s → 3pσ^* (RC*OH) and 286.7 eV for K 1s → π^* (R(C*═O)R or C*OH). The alcohol presumably comes from polysaccharides, and the carbonyl group is possibly attributed to acetylated polysaccharides. The second phytoplankton bloom overlapped with the heterotrophic bacteria bloom and most likely led to the incorporation of cellular components of bacteria into sea spray aerosols. As shown in the pie charts in Figure 3, during the prebloom and first bloom periods, the RC*OH transition was enhanced in larger particles. Colocated measurements of oligo/polysaccharides showed that saccharides were enriched in SSAs during IMPACTS, representing roughly 11% and 27% of the fine (D_a < 2.5 μm) and coarse (2.5 < D_a < 10 μm) organic mass.[53] Furthermore, the C*OH transition was observed to be enhanced in fine particles during the second bloom; concurrently, a maximum of saccharides in SSAs relative to seawater were observed by Jayarathne et al.[53]

Spectral deconvolution was performed for standard compounds to demonstrate the ability of NEXAFS to identify biologically relevant molecules (Figure S9). Sodium alginate, galactose, and *N*-acetylglucosamine are common saccharides that contain the alcohol functionality. Their spectra are dominated by the alcohol transition, but the spectra from the IMPACTS study shown in Figure 3 do not have well-resolved alcohol peaks. This suggests that polysaccharides were not present in a large enough abundance to be resolved in the NEXAFS spectra. However, the RC*OH peak was still used in deconvolution and accounted for 16−26% of the organic functional group intensity (Figure 3). The results here demonstrate that the spectral deconvolution provides a reasonable estimation of the relative trends for the saccharide and amide contributions that is consistent with other studies of SSA.[16,53]

3.4. Organic Volume Fractions (OVFs). Marine aerosols consist primarily of sea salt−organic particles, but during periods of high biological activity, some (but not all) studies have observed an increase in organic content.[9,53,54] OVFs are key data used in quantitatively evaluating hygroscopicity for inorganic−organic mixtures. Organic volume fractions were calculated here using STXM but can also be obtained using atomic force microscopy, which is a work in progress for the IMPACTS study. Using absorbance values at the pre-edge and post-edge and assuming a binary mixture of organic (adipic acid) and inorganic (NaCl) materials, OVFs were determined on a single-particle basis. Regions of the particles containing graphitic carbon were excluded from the OVF calculation. The sensitivity of the volume fraction calculation for a variety of organics besides adipic acid was tested as shown in Figure S11. Even though different values were used for the densities corresponding to the different organics tested in Figure S11, when the mass absorption coefficients corresponding to each of the species were taken into account, the OVF calculated was not sensitive to which organic species was used for the calculation. OVFs for specific particle types are presented in Figure S10 and Table S3 and as a function of bloom conditions and size in Figure 5.

Particles in the smallest size range have the largest OVFs because of the role that organics play in film drop production during bubble bursting. The mean OVF for the 0.18−0.32 μm size range increased from 0.38 ± 0.17 for the prebloom period to 0.62 ± 0.17 for the first bloom and then decreased to 0.42 ± 0.14 for the second bloom. The OVF distribution for the first bloom was bimodal with modes occurring at OVFs of 0.5 and 0.8 (Figure 5). The large organic enrichment during the first bloom was observed only for the 0.18−0.32 μm size range and corresponds to increased labile aliphatic hydrocarbons. Even for sea salt−organic particles the OVF is enhanced during the first bloom compared with the other bloom conditions (Figure S10). During the second bloom, the mean OVF distribution was skewed to slightly higher values because of higher levels of more oxidized organics.

The particle population in the 0.56−1 μm size range was dominated by organic-coated sea salt−organic particles, having a mean OVF of 0.34 ± 0.07 during the second bloom. This was not significantly different from prebloom conditions (0.36 ± 0.08; Table S3). However, the mean OVF of sea salt−organic particles for this size range was slightly lower for the first phytoplankton bloom (0.30 ± 0.14) compared with the prebloom and second bloom periods. As shown in Figure 5, the volume fraction distribution for the first bloom at this size range has two populations of particles, sea salt−organic particles with the mode near 0.2 and a very small population of organic-rich particles (homogeneous organics, Figure S10) with the mode near 0.7. The lower mean OVF for 0.56−1 μm sea salt−organic particles during the first phytoplankton bloom (Figure S10 and Table S3) may be a result of scavenging of organics by rising bubbles, resulting in a competitive partitioning between small (0.18−0.32 μm) and intermediate-sized (0.56−1 μm) particles.

The modal OVF for sea salt−organic particles with sizes of >1.8 μm was 0.05 for all bloom conditions. Unlike the sea salt−organic particles observed in the size range 0.56−1 μm, much of the organic portion in the 1.8−3.2 μm size range was associated with ordered "needlelike" structures, frequently

DOI: 10.1021/acsearthspacechem.7b00069
ACS Earth Space Chem. 2017, 1, 551−561

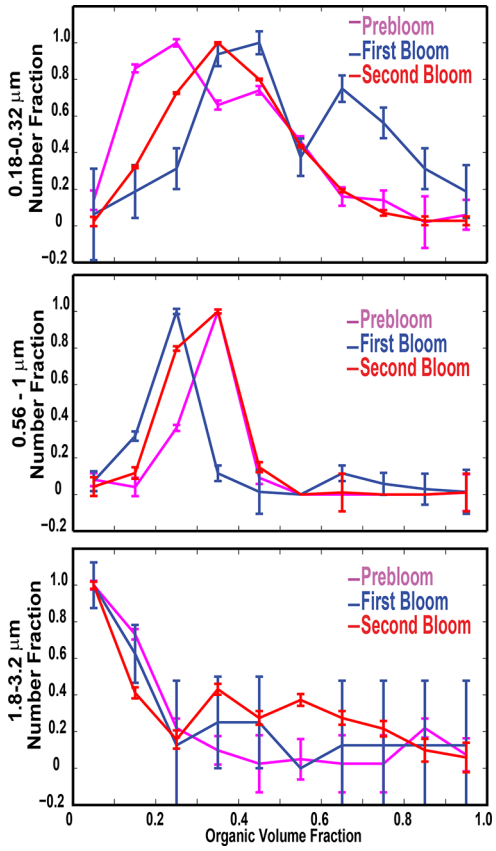

Figure 5. Organic volume fraction distributions as functions of bloom conditions and size. For the first bloom in the size range 1.8−3.2 μm, a size exclusion of >2 μm was imposed to exclude smaller particles that may have resulted from particle shattering. As a result, the systematic error associated with the first bloom in the size range 1.8−3.2 μm is potentially quite high because of the low number of particles. Consequently, a bulk organic volume fraction of 0.25 ± 0.21 was calculated instead for the first bloom in the size range 1.8−3.2 μm. The organic volume fraction for the size range 0.18−0.32 μm includes only particles for which full carbon K-edge spectra were available in order to exclude graphitic contributions.

outlining calcium-rich spines. Needlelike particles had large variation in OVF (0.1−0.7), as some were primarily calcium while others had calcium-containing inorganic species but were also heavily coated with carboxylic acid-rich organics. Both Raman spectroscopy and SEM confirmed that these rods were composed of calcium sulfate in addition to the carboxylic acid-rich organics identified through STXM. While prebloom and second bloom conditions primarily produced intact sea salt−organic particles, particles produced during the first bloom exhibited a high degree of fractionary recrystallization and particle shattering.[36] As a result, there were many particles with sizes of <3 μm during the first bloom, and these particles tended to be rich in either calcium, carboxylic acid-containing organics, or both. A bulk OVF (mass-weighted, including all particles) was calculated to be 0.25 ± 0.21 for large (1.8−3.2 μm) particles sampled during the first bloom. The large uncertainty in these numbers is due to the limited number of particles measured for this size range. The organic carbon mass fraction for coarse aerosol (2.5 < D_a < 10 μm) was determined to be 0.016 in the work by Jayarathne et al.[53] However, the size ranges for coarse aerosol in this work and the Jayarathne study are different and not directly comparable. Here the calculated OMF seems to be significantly higher than would be expected given the mass fractions published by Jayarathne et al., although the range of uncertainty for the STXM measurements is quite large.

3.5. Implications for Aerosol Hygroscopicity. OVFs derived from STXM measurements were used to calculate particle hygroscopicity using the κ formalism of Petters and Kreidenweis.[2] It was assumed that the particles are composed of two types of materials, organic and inorganic, that have distinct κ values. Inorganics were assumed to be NaCl and organics were assumed to be adipic acid for the purposes of these calculations. Adipic acid was chosen to represent oxidized organic matter on the basis of the characteristics of the NEXAFS spectra observed here and oxygen to carbon ratios for atmospheric particulate matter.[55] The κ values for adipic acid and NaCl are 0.006 and 1.12, respectively.[2] The κ values for specific particle types and size ranges are given in Table S4. Since the in situ CRD measurements used optically measured growth factors to derive κ, the resulting values are "optically weighted", meaning that the κ value is largely influenced by particle sizes that influence scattering the most (D_p ~ 500 nm). The optically weighted κ was calculated from J individual particles as follows (eq 3):

$$\kappa = \sum_i w_i \frac{\sum_j [(1 - f_{\mathrm{org},i,j})\kappa_{\mathrm{inorg}} + f_{\mathrm{org},i,j}\kappa_{\mathrm{org}}]}{J} \quad (3)$$

where $f_{\mathrm{org},i,j}$ is the OVF determined here, κ_{org} is taken as the value for adipic acid, and κ_{inorg} is taken to be that of NaCl. A weighting function (w_i) was used to convert the single-particle hygroscopicities in the different size bins to an average value that can be compared with the in situ optical observations. The in situ observations are scattering-weighted, as they were determined from the influence of water uptake on particle scattering, i.e., from measurements of f(RH). The observed particle number distribution, (dN/d log D_p), was first converted to a dry particle scattering distribution, (db_{sca}/d log D_p), where b_{sca} is the scattering coefficient, by multiplying by the calculated size-dependent cross section from Mie theory. The weighting function was calculated by normalizing the db_{sca}/d log D_p distributions to have an area of unity. In this way, κ values were calculated for each of the bloom conditions using the organic volume fractions obtained here. These values are compared with κ values derived from growth factors obtained using cavity ringdown spectroscopy. The κ values calculated with eq 3 are shown in Figure S12.

For different bloom conditions, the STXM-derived κ remains relatively constant (~0.72), whereas the κ values derived from cavity ringdown demonstrate more variation (Figure S12). Except for the prebloom, the κ values derived by the two techniques agreed within the levels of uncertainty. The unchanging nature of the STXM-derived κ is due to the relatively constant OVF for the 0.56−1 μm size range, which was given the largest optical weighting. For the prebloom period, the κ derived from the STXM measurements was significantly lower than that obtained using cavity ringdown. Reasons for this may include the following: (1) the organic volume fraction measured by STXM is systematically too high, possibly because of inorganic carbon; (2) the κ values assumed for the inorganic and organic components were not appropriate; and (3) differences between D_a and D_p.[56,57] Recent observations have implicated surface tension depression due to surface-active organics as leading to enhanced CCN

DOI: 10.1021/acsearthspacechem.7b00069
ACS Earth Space Chem. 2017, 1, 551−561

activity of mixed salt−organic particles. However, surface tension depression has a minimal influence on water uptake at RH values well below 100% (e.g., at 85%) and is thus less relevant to consider in the context of subsaturated hygroscopic growth. As the prebloom period represents conditions under which oxidized nonlabile organics are expected to dominate the organic composition, it is likely that adipic acid is a poor proxy for these types of organics, which may have higher hygroscopicities.

The lack of change in the OVF and composition of the intermediate particle sizes from prebloom to the second bloom demonstrates the importance of the ever-present pool of latent organics rich in carboxylic acids. These results demonstrate the vast contrasting complexities of carbon in SSA released during three differing seawater bloom conditions. Through continued study of similar systems, the effects of ocean biology on SSAs should lead to more predictable SSA carbonaceous speciation and physical properties.

■ ASSOCIATED CONTENT

Supporting Information

The Supporting Information is available free of charge on the ACS Publications website at DOI: 10.1021/acsearthspacechem.7b00069.

Additional details, Figures S1−S13, and Tables S1−S4 (PDF)

■ AUTHOR INFORMATION

Corresponding Author

*E-mail: rmoffet@pacific.edu.

ORCID

Camille Sultana: 0000-0003-4038-5518

Vicki Grassian: 0000-0001-5052-0045

Ryan C. Moffet: 0000-0002-2352-5454

Present Address

[▽]R.O.: Department of Civil and Environmental Engineering, Massachusetts Institute of Technology, Cambridge, Massachusetts 02139, United States.

Notes

The authors declare no competing financial interest.

■ ACKNOWLEDGMENTS

This work was supported by the National Science Foundation through the Centers of Chemical Innovation Program via the Center for Aerosol Impacts on Climate and the Environment (CAICE) (CHE-1305427). The authors acknowledge Jonathan V. Trueblood for sample collection. The authors thank Dale Stokes, Grant B. Deane, the staff at the SIO Hydraulics Laboratory, and all of their collaborators from CAICE for their IMPACTS. The authors thank David Kilcoyne for his support at beamline 5.3.2.2 at Lawrence Berkeley National Laboratory. The Advanced Light Source is supported by the Director, Office of Science, Office of Basic Energy Sciences, U.S. Department of Energy under Contract DE-AC02-05CH11231.

■ REFERENCES

(1) Boucher, O.; Randall, D.; Artaxo, P.; Bretherton, C.; Feingold, G.; Forster, P.; Kerminen, V.-M.; Kondo, Y.; Liao, H.; Lohmann, U.; Rasch, P.; Satheesh, S.K.; Sherwood, S.; Stevens, B.; Zhang, X.Y. Clouds and Aerosols. In *Climate Change 2013: The Physical Science Basis. Contribution of Working Group I to the Fifth Assessment Report of the Intergovernmental Panel on Climate Change*; Cambridge University Press: Cambridge, U.K., 2013.

(2) Petters, M. D.; Kreidenweis, S. M. A single parameter representation of hygroscopic growth and cloud condensation nucleus activity. *Atmos. Chem. Phys.* **2007**, *7* (8), 1961−1971.

(3) McCluskey, C. S.; Hill, T. C. J.; Malfatti, F.; Sultana, C. M.; Lee, C.; Santander, M. V.; Beall, C. M.; Moore, K. A.; Cornwell, G. C.; Collins, D. B.; Prather, K. A.; Jayarathne, T.; Stone, E. A.; Azam, F.; Kreidenweis, S. M.; DeMott, P. J. A Dynamic Link between Ice Nucleating Particles Released in Nascent Sea Spray Aerosol and Oceanic Biological Activity during Two Mesocosm Experiments. *J. Atmos. Sci.* **2017**, *74* (1), 151−166.

(4) Schill, S. R.; Collins, D. B.; Lee, C.; Morris, H. S.; Novak, G. A.; Prather, K. A.; Quinn, P. K.; Sultana, C. M.; Tivanski, A. V.; Zimmermann, K.; Cappa, C. D.; Bertram, T. H. The Impact of Aerosol Particle Mixing State on the Hygroscopicity of Sea Spray Aerosol. *ACS Cent. Sci.* **2015**, *1* (3), 132−141.

(5) Ault, A. P.; Moffet, R. C.; Baltrusaitis, J.; Collins, D. B.; Ruppel, M. J.; Cuadra-Rodriguez, L. A.; Zhao, D.; Guasco, T. L.; Ebben, C. J.; Geiger, F. M.; Bertram, T. H.; Prather, K. A.; Grassian, V. H. Size-Dependent Changes in Sea Spray Aerosol Composition and Properties with Different Seawater Conditions. *Environ. Sci. Technol.* **2013**, *47* (11), 5603−5612.

(6) Hawkins, L. N.; Russell, L. M. Polysaccharides, Proteins, and Phytoplankton Fragments: Four Chemically Distinct Types of Marine Primary Organic Aerosol Classified by Single Particle Spectromicroscopy. *Adv. Meteorol.* **2010**, *2010*, 612132.

(7) Blanchard, D. C. Bubble scavenging and the water-to-air transfer of organic material in the sea. *Adv. Chem.* **1975**, *145*, 360−387.

(8) Wang, X. F.; Deane, G. B.; Moore, K. A.; Ryder, O. S.; Stokes, M. D.; Beall, C. M.; Collins, D. B.; Santander, M. V.; Burrows, S. M.; Sultana, C. M.; Prather, K. A. The role of jet and film drops in controlling the mixing state of submicron sea spray aerosol particles. *Proc. Natl. Acad. Sci. U. S. A.* **2017**, *114* (27), 6978−6983.

(9) O'Dowd, C. D.; Facchini, M. C.; Cavalli, F.; Ceburnis, D.; Mircea, M.; Decesari, S.; Fuzzi, S.; Yoon, Y. J.; Putaud, J. P. Biogenically driven organic contribution to marine aerosol. *Nature* **2004**, *431* (7009), 676−680.

(10) Blanchard, D. C. The ejection of drops from the sea and their enrichment with bacteria and other materials: a review. *Estuaries* **1989**, *12* (3), 127−137.

(11) Prather, K. A.; Bertram, T. H.; Grassian, V. H.; Deane, G. B.; Stokes, M. D.; DeMott, P. J.; Aluwihare, L. I.; Palenik, B. P.; Azam, F.; Seinfeld, J. H.; Moffet, R. C.; Molina, M. J.; Cappa, C. D.; Geiger, F. M.; Roberts, G. C.; Russell, L. M.; Ault, A. P.; Baltrusaitis, J.; Collins, D. B.; Corrigan, C. E.; Cuadra-Rodriguez, L. A.; Ebben, C. J.; Forestieri, S. D.; Guasco, T. L.; Hersey, S. P.; Kim, M. J.; Lambert, W. F.; Modini, R. L.; Mui, W.; Pedler, B. E.; Ruppel, M. J.; Ryder, O. S.; Schoepp, N. G.; Sullivan, R. C.; Zhao, D. Bringing the ocean into the laboratory to probe the chemical complexity of sea spray aerosol. *Proc. Natl. Acad. Sci. U. S. A.* **2013**, *110* (19), 7550−7555.

(12) Leck, C.; Norman, M.; Bigg, E. K.; Hillamo, R. Chemical composition and sources of the high Arctic aerosol relevant for cloud formation. *J. Geophys. Res.* **2002**, *107* (D12), AAC 1.

(13) Collins, D. B.; Zhao, D. F.; Ruppel, M. J.; Laskina, O.; Grandquist, J. R.; Modini, R. L.; Stokes, M. D.; Russell, L. M.; Bertram, T. H.; Grassian, V. H.; Deane, G. B.; Prather, K. A. Direct aerosol chemical composition measurements to evaluate the physicochemical differences between controlled sea spray aerosol generation schemes. *Atmos. Meas. Tech.* **2014**, *7* (11), 3667−3683.

(14) Stokes, M. D.; Deane, G. B.; Prather, K.; Bertram, T. H.; Ruppel, M. J.; Ryder, O. S.; Brady, J. M.; Zhao, D. A Marine Aerosol Reference Tank system as a breaking wave analogue for the production of foam and sea-spray aerosols. *Atmos. Meas. Tech.* **2013**, *6* (4), 1085−1094.

(15) *Biogeochemistry of Marine Dissolved Organic Matter*, 2nd ed.; Hansell, D. A., Carlson, C. A., Eds.; Academic Press: San Diego, CA, 2015.

DOI: 10.1021/acsearthspacechem.7b00069
ACS Earth Space Chem. 2017, 1, 551−561

(16) Quinn, P. K.; Collins, D. B.; Grassian, V. H.; Prather, K. A.; Bates, T. S. Chemistry and related properties of freshly emitted sea spray aerosol. *Chem. Rev.* **2015**, *115* (10), 4383−99.
(17) Hertkorn, N.; Benner, R.; Frommberger, M.; Schmitt-Kopplin, P.; Witt, M.; Kaiser, K.; Kettrup, A.; Hedges, J. I. Characterization of a major refractory component of marine dissolved organic matter. *Geochim. Cosmochim. Acta* **2006**, *70* (12), 2990−3010.
(18) Abdulla, H. A. N.; Minor, E. C.; Hatcher, P. G. Using Two-Dimensional Correlations of C-13 NMR and FTIR To Investigate Changes in the Chemical Composition of Dissolved Organic Matter along an Estuarine Transect. *Environ. Sci. Technol.* **2010**, *44* (21), 8044−8049.
(19) Haberstroh, P. R.; Brandes, J. A.; Gelinas, Y.; Dickens, A. F.; Wirick, S.; Cody, G. Chemical composition of the graphitic black carbon fraction in riverine and marine sediments at sub-micron scales using carbon X-ray spectromicroscopy. *Geochim. Cosmochim. Acta* **2006**, *70* (6), 1483−1494.
(20) *Microbial Ecology of the Oceans*, 2nd ed.; Kirchman, D. L., Ed.; Wiley: Hoboken, NJ, 2008.
(21) Wang, X. F.; Sultana, C. M.; Trueblood, J.; Hill, T. C. J.; Malfatti, F.; Lee, C.; Laskina, O.; Moore, K. A.; Beall, C. M.; McCluskey, C. S.; Cornwell, G. C.; Zhou, Y. Y.; Cox, J. L.; Pendergraft, M. A.; Santander, M. V.; Bertram, T. H.; Cappa, C. D.; Azam, F.; DeMott, P. J.; Grassian, V. H.; Prather, K. A. Microbial Control of Sea Spray Aerosol Composition: A Tale of Two Blooms. *ACS Cent. Sci.* **2015**, *1* (3), 124−131.
(22) Leck, C.; Bigg, E. K. Source and evolution of the marine aerosol - A new perspective. *Geophys. Res. Lett.* **2005**, *32* (19), L19803.
(23) Silhavy, T. J.; Kahne, D.; Walker, S. The Bacterial Cell Envelope. *Cold Spring Harbor Perspect. Biol.* **2010**, *2* (5), a000414.
(24) Guillard, R. R.; Ryther, J. H. Studies of marine planktonic diatoms. I. Cyclotella nana Hustedt, and Detonula confervacea (cleve) Gran. *Can. J. Microbiol.* **1962**, *8*, 229−39.
(25) Kilcoyne, A. L. D.; Tyliszczak, T.; Steele, W. F.; Fakra, S.; Hitchcock, P.; Franck, K.; Anderson, E.; Harteneck, B.; Rightor, E. G.; Mitchell, G. E.; Hitchcock, A. P.; Yang, L.; Warwick, T.; Ade, H. Interferometer-controlled scanning transmission X-ray microscopes at the Advanced Light Source. *J. Synchrotron Radiat.* **2003**, *10*, 125−136.
(26) Moffet, R. C.; Henn, T.; Laskin, A.; Gilles, M. K. Automated Chemical Analysis of Internally Mixed Aerosol Particles Using X-ray Spectromicroscopy at the Carbon K-Edge. *Anal. Chem.* **2010**, *82* (19), 7906−7914.
(27) Tivanski, A. V.; Hopkins, R. J.; Tyliszczak, T.; Gilles, M. K. Oxygenated interface on biomass burn tar balls determined by single particle scanning transmission X-ray microscopy. *J. Phys. Chem. A* **2007**, *111* (25), 5448−5458.
(28) DeCarlo, P. F.; Kimmel, J. R.; Trimborn, A.; Northway, M. J.; Jayne, J. T.; Aiken, A. C.; Gonin, M.; Fuhrer, K.; Horvath, T.; Docherty, K. S.; Worsnop, D. R.; Jimenez, J. L. Field-deployable, high-resolution, time-of-flight aerosol mass spectrometer. *Anal. Chem.* **2006**, *78* (24), 8281−8289.
(29) Ulbrich, I. M.; Canagaratna, M. R.; Zhang, Q.; Worsnop, D. R.; Jimenez, J. L. Interpretation of organic components from Positive Matrix Factorization of aerosol mass spectrometric data. *Atmos. Chem. Phys.* **2009**, *9* (9), 2891−2918.
(30) Forestieri, S. D.; Cornwell, G. C.; Helgestad, T. M.; Moore, K. A.; Lee, C.; Novak, G. A.; Sultana, C. M.; Wang, X. F.; Bertram, T. H.; Prather, K. A.; Cappa, C. D. Linking variations in sea spray aerosol particle hygroscopicity to composition during two microcosm experiments. *Atmos. Chem. Phys.* **2016**, *16* (14), 9003−9018.
(31) Cappa, C. D.; Onasch, T. B.; Massoli, P.; Worsnop, D. R.; Bates, T. S.; Cross, E. S.; Davidovits, P.; Hakala, J.; Hayden, K. L.; Jobson, B. T.; Kolesar, K. R.; Lack, D. A.; Lerner, B. M.; Li, S.-M.; Mellon, D.; Nuaaman, I.; Olfert, J. S.; Petaja, T.; Quinn, P. K.; Song, C.; Subramanian, R.; Williams, E. J.; Zaveri, R. A. Radiative Absorption Enhancements Due to the Mixing State of Atmospheric Black Carbon. *Science* **2012**, *337* (6098), 1078−1081.
(32) Langridge, J. M.; Richardson, M. S.; Lack, D.; Law, D.; Murphy, D. M. Aircraft Instrument for Comprehensive Characterization of Aerosol Optical Properties, Part I: Wavelength-Dependent Optical Extinction and Its Relative Humidity Dependence Measured Using Cavity Ringdown Spectroscopy. *Aerosol Sci. Technol.* **2011**, *45* (11), 1305−1318.
(33) Hinds, W. C. *Aerosol Technology*; Wiley: New York, 1999.
(34) Moffet, R. C.; Qin, X. Y.; Rebotier, T.; Furutani, H.; Prather, K. A. Chemically segregated optical and microphysical properties of ambient aerosols measured in a single-particle mass spectrometer. *J. Geophys. Res.* **2008**, *113* (D12), D12213.
(35) Marple, V. A.; Liu, B. Y. H.; Kuhlmey, G. A. A Uniform Deposit Impactor. *J. Aerosol Sci.* **1981**, *12* (4), 333−337.
(36) Mouri, H.; Okada, K. Shattering and Modification of Sea-Salt Particles in the Marine Atmosphere. *Geophys. Res. Lett.* **1993**, *20* (1), 49−52.
(37) Cochran, R. E.; Laskina, O.; Jayarathne, T.; Laskin, A.; Laskin, J.; Lin, P.; Sultana, C.; Lee, C.; Moore, K. A.; Cappa, C. D.; Bertram, T. H.; Prather, K. A.; Grassian, V. H.; Stone, E. A. Analysis of Organic Anionic Surfactants in Fine and Coarse Fractions of Freshly Emitted Sea Spray Aerosol. *Environ. Sci. Technol.* **2016**, *50* (5), 2477−2486.
(38) Cochran, R. E.; Jayarathne, T.; Stone, E. A.; Grassian, V. H. Selectivity Across the Interface: A Test of Surface Activity in the Composition of Organic-Enriched Aerosols from Bubble Bursting. *J. Phys. Chem. Lett.* **2016**, *7* (9), 1692−1696.
(39) Brandes, J. A.; Lee, C.; Wakeham, S.; Peterson, M.; Jacobsen, C.; Wirick, S.; Cody, G. Examining marine particulate organic matter at sub-micron scales using scanning transmission X-ray microscopy and carbon X-ray absorption near edge structure spectroscopy. *Mar. Chem.* **2004**, *92* (1−4), 107−121.
(40) Moffet, R. C.; Henn, T. R.; Tivanski, A. V.; Hopkins, R. J.; Desyaterik, Y.; Kilcoyne, A. L. D.; Tyliszczak, T.; Fast, J.; Barnard, J.; Shutthanandan, V.; Cliff, S. S.; Perry, K. D.; Laskin, A.; Gilles, M. K. Microscopic characterization of carbonaceous aerosol particle aging in the outflow from Mexico City. *Atmos. Chem. Phys.* **2010**, *10* (3), 961−976.
(41) Braun, A.; Kubatova, A.; Wirick, S.; Mun, S. B. Radiation damage from EELS and NEXAFS in diesel soot and diesel soot extracts. *J. Electron Spectrosc. Relat. Phenom.* **2009**, *170* (1−3), 42−48.
(42) Novakova, E.; Mitrea, G.; Peth, C.; Thieme, J.; Mann, K.; Salditt, T. Solid supported multicomponent lipid membranes studied by x-ray spectromicroscopy. *Biointerphases* **2008**, *3* (2), FB44−FB54.
(43) Myneni, S. C. B. Soft X-Ray Spectroscopy and Spectromicroscopy of Organic Molecules in the Environment. *Rev. Mineral. Geochem.* **2002**, *49*, 485−579.
(44) Stöhr, J. *NEXAFS Spectroscopy*; U.S. Government Printing Office: Washington, DC, 1992.
(45) Cochran, R. E.; Laskina, O.; Trueblood, J.; Estillore, A. D.; Morris, H. S.; Jayarathne, T.; Sultana, C. M.; Lee, C.; Lin, P.; Laskin, J.; Laskin, A.; Dowling, J. A.; Qin, Z.; Cappa, C. D.; Bertram, T. H.; Tivanski, A. V.; Stone, E. A.; Prather, K.; Grassian, V. H. Molecular Diversity of Sea Spray Aerosol Particles: Impact of Ocean Biology on Particle Composition and Hygroscopicity. *Chem.* **2017**, *2*, 655−667.
(46) Budge, S. M.; Devred, E.; Forget, M.-H.; Stuart, V.; Trzcinski, M. K.; Sathyendranath, S.; Platt, T. Estimating concentrations of essential omega-3 fatty acids in the ocean: supply and demand. *ICES J. Mar. Sci.* **2014**, *71* (7), 1885−1893.
(47) Ehlert, C.; Unger, W. E. S.; Saalfrank, P. C K-edge NEXAFS spectra of graphene with physical and chemical defects: a study based on density functional theory. *Phys. Chem. Chem. Phys.* **2014**, *16* (27), 14083−14095.
(48) Park, J. Y.; Lim, S.; Park, K. Mixing State of Submicrometer Sea Spray Particles Enriched by Insoluble Species in Bubble-Bursting Experiments. *J. Atmos Ocean Tech* **2014**, *31* (1), 93−104.
(49) Russell, L. M.; Hawkins, L. N.; Frossard, A. A.; Quinn, P. K.; Bates, T. S. Carbohydrate-like composition of submicron atmospheric particles and their production from ocean bubble bursting. *Proc. Natl. Acad. Sci. U. S. A.* **2010**, *107* (15), 6652−6657.
(50) Tang, C. Y.; Huang, Z. S.; Allen, H. C. Interfacial Water Structure and Effects of Mg2+ and Ca2+ Binding to the COOH

DOI: 10.1021/acsearthspacechem.7b00069
ACS Earth Space Chem. 2017, 1, 551−561

Headgroup of a Palmitic Acid Monolayer Studied by Sum Frequency Spectroscopy. *J. Phys. Chem. B* **2011**, *115* (1), 34−40.
(51) Freedman, M. A.; Hasenkopf, C. A.; Beaver, M. R.; Tolbert, M. A. Optical Properties of Internally Mixed Aerosol Particles Composed of Dicarboxylic Acids and Ammonium Sulfate. *J. Phys. Chem. A* **2009**, *113* (48), 13584−13592.
(52) Solomon, D.; Lehmann, J.; Harden, J.; Wang, J.; Kinyangi, J.; Heymann, K.; Karunakaran, C.; Lu, Y. S.; Wirick, S.; Jacobsen, C. Micro- and nano-environments of carbon sequestration: Multi-element STXM-NEXAFS spectromicroscopy assessment of microbial carbon and mineral associations. *Chem. Geol.* **2012**, *329*, 53−73.
(53) Jayarathne, T.; Sultana, C. M.; Lee, C.; Malfatti, F.; Cox, J. L.; Pendergraft, M. A.; Moore, K. A.; Azam, F.; Tivanski, A. V.; Cappa, C. D.; Bertram, T. H.; Grassian, V. H.; Prather, K. A.; Stone, E. A. Enrichment of Saccharides and Divalent Cations in Sea Spray Aerosol During Two Phytoplankton Blooms. *Environ. Sci. Technol.* **2016**, *50* (21), 11511−11520.
(54) Quinn, P. K.; Bates, T. S.; Schulz, K. S.; Coffman, D. J.; Frossard, A. A.; Russell, L. M.; Keene, W. C.; Kieber, D. J. Contribution of sea surface carbon pool to organic matter enrichment in sea spray aerosol. *Nat. Geosci.* **2014**, *7* (3), 228−232.
(55) Jimenez, J. L.; Canagaratna, M. R.; Donahue, N. M.; Prevot, A. S. H.; Zhang, Q.; Kroll, J. H.; DeCarlo, P. F.; Allan, J. D.; Coe, H.; Ng, N. L.; Aiken, A. C.; Docherty, K. S.; Ulbrich, I. M.; Grieshop, A. P.; Robinson, A. L.; Duplissy, J.; Smith, J. D.; Wilson, K. R.; Lanz, V. A.; Hueglin, C.; Sun, Y. L.; Tian, J.; Laaksonen, A.; Raatikainen, T.; Rautiainen, J.; Vaattovaara, P.; Ehn, M.; Kulmala, M.; Tomlinson, J. M.; Collins, D. R.; Cubison, M. J.; Dunlea, E. J.; Huffman, J. A.; Onasch, T. B.; Alfarra, M. R.; Williams, P. I.; Bower, K.; Kondo, Y.; Schneider, J.; Drewnick, F.; Borrmann, S.; Weimer, S.; Demerjian, K.; Salcedo, D.; Cottrell, L.; Griffin, R.; Takami, A.; Miyoshi, T.; Hatakeyama, S.; Shimono, A.; Sun, J. Y.; Zhang, Y. M.; Dzepina, K.; Kimmel, J. R.; Sueper, D.; Jayne, J. T.; Herndon, S. C.; Trimborn, A. M.; Williams, L. R.; Wood, E. C.; Middlebrook, A. M.; Kolb, C. E.; Baltensperger, U.; Worsnop, D. R. Evolution of Organic Aerosols in the Atmosphere. *Science* **2009**, *326* (5959), 1525−1529.
(56) Ovadnevaite, J.; Zuend, A.; Laaksonen, A.; Sanchez, K. J.; Roberts, G.; Ceburnis, D.; Decesari, S.; Rinaldi, M.; Hodas, N.; Facchini, M. C.; Seinfeld, J. H.; O'Dowd, C. Surface tension prevails over solute effect in organic-influenced cloud droplet activation. *Nature* **2017**, *546* (7660), 637−641.
(57) Ruehl, C. R.; Davies, J. F.; Wilson, K. R. An interfacial mechanism for cloud droplet formation on organic aerosols. *Science* **2016**, *351* (6280), 1447−1450.

DOI: 10.1021/acsearthspacechem.7b00069
ACS Earth Space Chem. 2017, 1, 551−561